Front. Earth Sci. 2023, 17(2): 604–619
https://doi.org/10.1007/s11707-021-0961-2

RESEARCH ARTICLE

Characteristics for the sources and sinks of gravity waves in an orographic heavy snowfall event

Shuping MA[1,2], Lingkun RAN (✉)[1,2], Jie CAO[1,3,4], Baofeng JIAO[1], Kuo ZHOU[1]

1 Key Laboratory of Cloud–Precipitation Physics and Severe Storms, Institute of Atmospheric Physics (LACS), Chinese Academy of Sciences, Beijing 100029, China
2 University of Chinese Academy of Sciences, Beijing 100049, China
3 Cooperative Institute for Mesoscale Meteorological Studies, University of Oklahoma, Norman OK 73072, USA
4 Key Laboratory of Meteorological Disaster (KLME), Ministry of Education & Collaborative Innovation Center on Forecast and Evaluation of Meteorological Disasters (CIC-FEMD), Nanjing University of Information Science & Technology, Nanjing 210044, China

Abstract The characteristics of the mesoscale gravity waves during a snowfall event on November 30, 2018 over the Ili Valley and the northern slope of the Tianshan Mountains are analyzed based on the Weather Research and Forecasting model simulation. The vertical distribution of *Ro* is similar to that of the residual of the nonlinear balance equation (ΔNBE), with their high-value areas located over the leeward slope and the fluctuations extending upwardly with time, indicating the characteristics of strong ageostrophy and non-equilibrium of atmospheric motions. In addition, the *Ro* and ΔNBE are first developed in the lower layers over the leeward slope, revealing that the generation of the gravity waves is closely related to the topography. Thus, the topographic uplifting greatly affects this snowfall, and the ageostrophic motion in the whole troposphere and the lower stratosphere, as well as the unbalanced motions between convergence and divergence over the peak and the leeward slope are conductive to the development of the inertia-gravity waves. In terms of the horizontal scale of the gravity waves, the Barnes' band-pass filter is applied to separate the mesoscale waves and the synoptic-scale basic flow. The vertical distributions of the vorticity and divergence perturbations have a phase difference of $\pi/2$, indicating the polarization state of gravity waves. The analyses on the sources and sinks of gravity waves by the non-hydrostatic wave equation show that the main forcing term for orographic gravity waves is the second-order nonlinear term, whose magnitude mainly depends on the nonlinear thermal forcing. This term is mainly related to the vertical transport of potential temperature perturbations. During the snowfall, the potential temperature perturbations are mainly caused by the topographic relief and the release of condensation latent heat. Therefore, the gravity waves in this snowfall are caused by the topographic forcing and condensation latent heating.

Keywords gravity wave, Fourier transform, nonlinear balance equation, non-hydrostatic wave equation

1 Introduction

The gravity waves, as fluctuations ubiquitous in the atmosphere, have a significant influence on the evolution of weather systems in the troposphere and stratosphere (Eliassen and Palm, 1960; Holton et al., 1995; Fritts and Alexander, 2003). The geostrophic adjustment, convective activities, shear instability and topography can all cause the generation of gravity waves (Bosart et al., 1998; Zhang et al., 2001; Zhang, 2004; Pandya et al., 2000; Kim et al., 2003). The obvious interaction between the convection and the gravity waves can be explained by the conditional instability of the second kind (CISK) mechanism. Lindzen (1974) pointed out that the wave-CISK mechanism can reasonably describe the positive feedback between the gravity waves and the strong convective activities. In other words, the gravity waves can cause the CISK without the Ekman pumping, which is called the wave-CISK. Moreover, the fluctuations caused by the CISK will certainly induce the cumulus activities. Additionally, the gravity waves induced by the topography propagate upwardly (Bruintjes et al., 1994; Garvert et al., 2007; Siler et al., 2013), with part of them passing through the tropopause into the stratosphere, part of them being absorbed near the tropopause, and the rest being reflected back in the upper layer and then

Received June 20, 2021; accepted December 2, 2021

E-mail: rlk@mail.iap.ac.cn

propagating downwardly (Eliassen and Palm, 1960). Therefore, the gravity waves are of great significance.

The orographic gravity waves are closely related to the orographic rainstorm (Garvert et al., 2007; Siler et al., 2013). Bruintjes et al. (1994) observed that the orographic gravity waves propagate upwardly and extend to the upper atmosphere at a considerable vertical velocity, sometimes exceeding 5 $m \cdot s^{-1}$, which enhances the vertical motion of the atmosphere and changes the distributions of cloud and precipitation through the enhanced seeder-feeder mechanism. Medina et al. (2005) revealed that the orographic gravity waves produce a strong downdraft over the leeward slope, resulting in the convergence of the airflow in the lower layers and further triggering the precipitation over the leeward slope of the downstream area. The orographic gravity wave is one of the key factors causing the orographic precipitation (Garvert et al., 2007; Houze, 2012; Siler et al., 2013). Zhang et al. (2001) pointed out that the geostrophic adjustment process excited by the ageostrophic wind near the upper-level jet can promote the occurrence and development of gravity waves. While Miles (1961) and Howard (1961) suggested that the gravity waves can get energy for development from the dynamic instability caused by the vertical wind shear.

The orographic drag is caused by the forces on the atmosphere from the flow over or around mountains, which is crucial to the atmospheric circulation (Sandu et al., 2019). In models with a relatively coarse horizontal grid spacing (20–150 km), the model dynamics cannot accurately represent the orographic effects at horizontal scales smaller than 3 to 8 times the grid spacing. Therefore, the orographic drag parametrizations should be used to represent the effects of unresolved orographic features on the atmospheric flow across a wide range of spatial scales, and should vary accordingly across all model grids. However, latest research (van Niekerk et al., 2016; Sandu et al., 2019; Vosper et al., 2020) has shown that models adopting the orographic drag parametrizations cannot obtain the desired results when the grid spacing is varied, and the representation of unresolved orographic drag processes within models remains uncertain (Sandu et al., 2019) due to the lack of observational or theoretical constraints on orographic drag within the troposphere and in the lower stratosphere at global or even at local scale. Several studies have found that the orography is better resolved in high-resolution simulations, and the atmospheric circulation is much better represented in high-resolution simulations than in model simulations with coarser grid spacing (e.g., Berckmans et al., 2013; Kanehama et al., 2019). At these resolutions, important orographic effects become resolved, and thus there is less need to parametrize them. Enhanced generation of gravity waves caused by resolving increasingly smaller orographic scales can propagate vertically, grow in amplitude, and have a significant nonlocal impact on large-scale circulations in the stratosphere and mesosphere (Fritts and Alexander, 2003). In addition, the mesoscale model WRF version 3.1 released in 2009 with the parameterization of Orographic Gravity Wave Drag (OGWD) being introduced is used to deal with the non-static model orographic gravity wave drag effect over complex terrain areas, thus making the simulation effect of orographic precipitation closer to the real situation (Liu et al., 2012). Therefore, the high-resolution WRF model has potential value in the study of gravity waves, and the high-resolution numerical simulation is an important way to capture and study the mesoscale gravity waves. O'sullivan and Dunkerton (1995) used a hemispheric model with the resolution of 100 km to simulate the synoptic-scale (600–1000 km) inertial gravity waves. Zhang (2004) analyzed the generation mechanism for mesoscale gravity waves through a high-resolution (3.3 km) numerical simulation. The results show that the mesoscale gravity waves are generated due to the balance adjustment, and the flow imbalance from the developing baroclinic waves leads to continuous gravity waves. The non-hydrostatic wave equation is the main method to analyze the sources and sinks of gravity waves (e.g., Ford, 1994; Plougonven and Zhang, 2007; Song et al., 2003; Wang and Zhang, 2010; Ran and Chen, 2016). Through the deduction of the wave equation, Ford (1994) revealed that the gravity waves are related to the nonlinear effect caused by the vortex motion. By studying the forcing from the large-scale basic flow on the inertial gravity waves, Plougonven and Zhang (2007) pointed out that the unbalanced motion has the main forcing effect on the generation of gravity waves. Song et al. (2003) proposed that the nonlinear forcing and diabatic forcing are the main sources for the generation of gravity waves, and the nonlinear forcing is 2–3 times as strong as the diabatic forcing. By using a linear numerical model, Wang and Zhang (2010) revealed that the gravity waves are mainly caused by the combined effect of the imbalance in the large-scale vorticity and divergence and the thermal forcing. Ran and Chen (2016) developed a non-hydrostatic wave equation to analyze the source and sink of mesoscale gravity waves, and suggested that the generation of gravity waves is closely related to the thermodynamic processes.

The Xinjiang Uygur Autonomous Region is located in the northwest of China, with a special topography of "two basins between three mountains", where the heavy rainfall in Xinjiang is mainly concentrated over the Ili Valley and the Tianshan Mountains. The snowfall acts as an important part in the precipitation in Xinjiang (Guan et al., 2016; Shang et al., 2018). It lasts more than 6 months every year, and the annual snowfall reaches 32.6 mm (Wang et al., 2020), where the amount in mountainous areas accounts for more than 80% of its total annual precipitation (Zhang and Deng, 1987). Studies have shown that the precipitation in Xinjiang is closely related

to the orographic gravity waves. For example, Yang et al. (2018) analyzed the characteristics of the gravity waves during a rainstorm over the Ili Valley from June 16 to 17, 2016. Are there any gravity wave activities during the snowfall processes in Xinjiang? What are their characteristics? What are the forcing terms (source/sink terms) for gravity waves? To answer these questions, the characteristics and generation mechanisms of the orographic gravity waves during a snowfall over the Ili Valley and the northern slope of the Tianshan Mountains from November 30 to December 2, 2018 are investigated in this study. This study aims to enhance the understanding of the topography-induced snowfall and gravity waves in Xinjiang and provide new ideas or perspectives for snowstorm forecasts in Xinjiang.

The remainder of this study is organized as follows. Section 2 introduces the data and methods. Section 3 gives a comparison between the simulations and the observations. Section 4 describes the characteristics of the gravity waves during this snowfall. Section 5 investigates the generation mechanism for the gravity waves. Finally, Section 6 provides the main conclusions.

2 Data and methods

The data sets used in this paper mainly include the precipitation observation data in China, 3-h data with the horizontal resolution of 0.5°×0.5° from the Global Forecast System of the National Centers for Environmental Prediction in the United States and the forecasts from the WRF (Weather Research and Forecasting) model.

The WRF4.0 model from the National Center for Atmospheric Research (Skamarock et al., 2019) is used to perform high-resolution numerical simulations of this snowfall process. The 3-h precipitation forecasts provide the background field and the lateral boundary conditions, and the GSI (Gridpoint Statistical Interpolation analysis system) is used to assimilate the GDAS (Global Data Assimilation System) observation data, with the horizontal resolution being 3 km and 44 layers in the vertical direction for model's output field centered at (46.5°N, 88°E), which output the results every 30 min. The initial forecasting time is set at 0000 UTC on November 30, 2018, with the forecast leading time of 48 h. The physical parameterization schemes adopted here are shown in Table 1. For more detailed setups and accuracy tests of this simulation, please refer to Ma et al. (2021).

Table 1 Mode scheme settings

Physical scheme	
Cloud microphysics scheme	Thompson cloud microphysics scheme
Longwave and shortwave radiation scheme	RRTMG/ RRTMG rapid radiative transfer model scheme
Planetary boundary layer scheme	Yonsei University scheme
Surface layer scheme	Mellor-Yamada-Janjic turbulent kinetic energy-based boundary layer scheme
Land-surface processes	Noah Land Surface Model

The fast Fourier transform (FFT) algorithm, Barnes' filter and non-hydrostatic wave equation (Ran and Chen, 2016) are used to investigate the characteristics and generation mechanisms for gravity waves.

3 Case overview

From 0000 UTC on November 30 to 0000 UTC on December 2, 2018, a snowfall with local heavy snowstorm occurred over the Ili Valley and the Tianshan Mountains in Xinjiang. This snowfall process began on the afternoon of November 30 and gradually strengthened with time. Afterwards, the snow center moved eastward, and the snow gradually weakened until its disappearance on December 2. There are two snowfall centers at 0000 UTC on December 1. One is located between the Ili River Valley and the southern slope of the Tianshan Mountains, and the other is between the Ili Valley and the northern slope of the Tianshan Mountains. The former snowfall center's 12-h accumulated snowfall is 8.4 mm, and the latter is 8 mm, reaching the magnitude of snowstorm respectively.

Figure 1 displays the simulations corresponding to the observations during the same period. In terms of the snowfall intensity, the simulation is slightly higher than the observation, but the location of the simulated snowfall center accords with the observation, along with similar ranges (Figs. 1(a) and 1(b)). The intensity of simulated water vapor fluxes at 700 hPa is weaker than the observation over the Ili River Valley, however, the position of convergence and distribution of water vapor fluxes are similar between the simulation and observation. In addition, the observed and simulated horizontal flow field at 850 hPa have almost the same distribution, both exhibiting a low-level jet with similar intensities. It indicates that the simulation can well reproduce the evolution of this snowfall event and the movement of the snow belt, and thus the model output is reliable. Therefore, these simulations are used to study the characteristics and evolution mechanism for the gravity waves during this snowfall.

4 Characteristics of the gravity waves

The mesoscale inertia-gravity waves are closely related to the heavy rainfall. Particularly, the topography-induced gravity waves can promote the local precipitation (Zhu et al., 1999; Medina et al., 2005; Garvert et al., 2007; Houze, 2012; Guo et al., 2013; Siler et al., 2013). The steep topographies of the Ili Valley and the northern and southern slopes of the Tianshan Mountains in Xinjiang can easily trigger the orographic gravity waves. Figure 2 shows the vertical distributions of wind speed at the initial, enhancing and weakening stages of the precipitation. When the

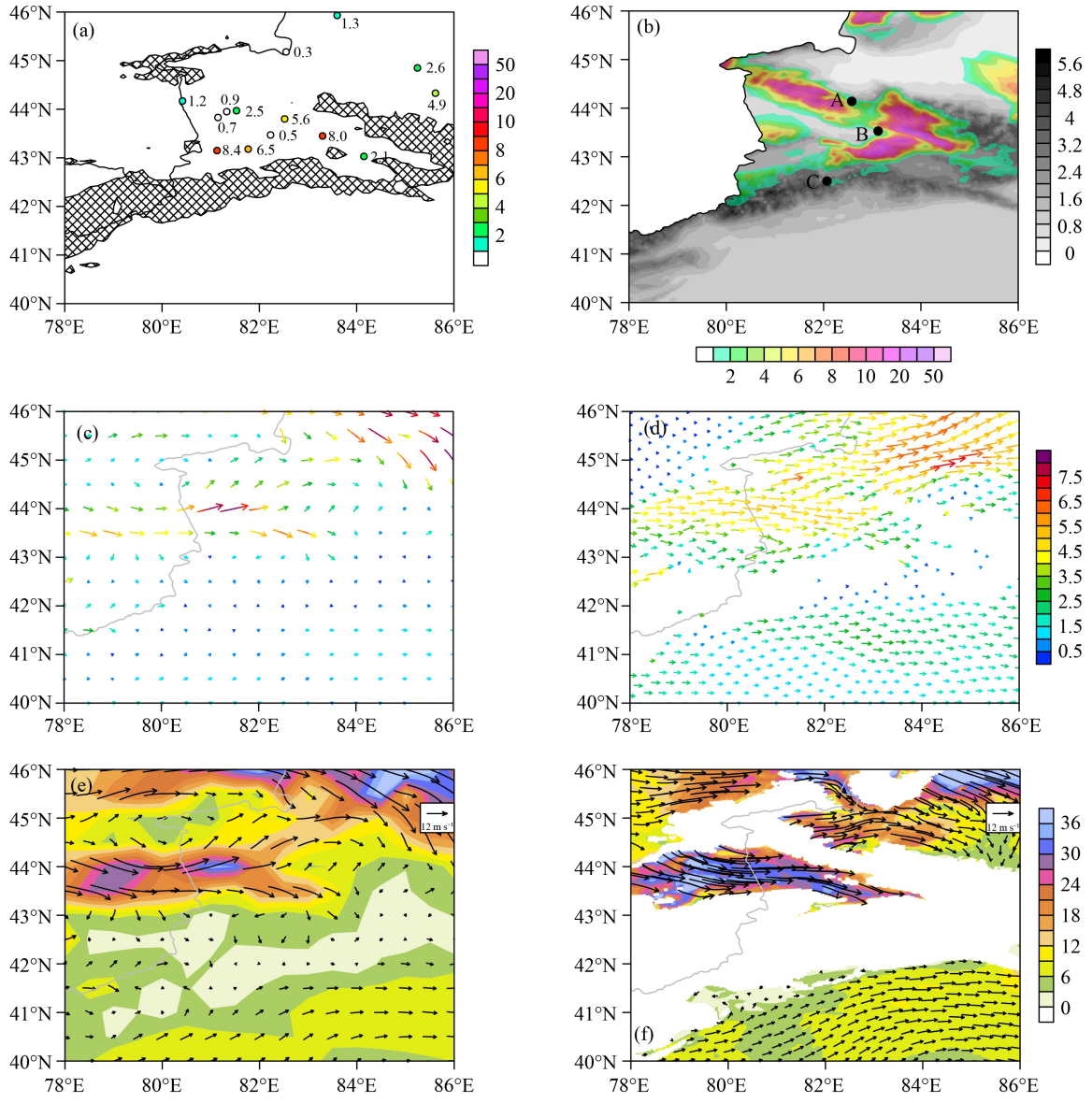

Fig. 1 (a) 12-h accumulated snowfall from observations (color dot, units: mm) at 0000 UTC on December 1, the grid area indicates where the terrain height is greater than 3 km; (b) 12-h accumulated snowfall from simulations (shading, units: mm), where the gray shading denotes the terrain height (units: km), the north-west-south-east gray shading near point A indicate the northern slope of the Tianshan Mountains, point B indicate the Ili Valley, and the south-west-north-east gray shading near point C indicate the southern slope of the Tianshan Mountains; 700hPa (c) observed and (d) simulated water vapor fluxes (units: $g \cdot cm^{-1} \cdot hPa^{-1} \cdot s^{-1}$) at 1800 UTC on Nov 30; 850hPa (e) observed and (f) simulated horizontal flow fields (arrows) and wind speed (shading, units: $m \cdot s^{-1}$) at 1800 UTC on November 30.

airflow passed over the mountain at 1330 UTC on November 30, 2018, the vertical motion on the windward slope was weak, while the ascending and descending motions over the peak and the leeward slope were strong. Till 1600 UTC, the vertical motion on the windward slope caused by the airflow over the mountain gradually strengthened with the enhancement and eastward movement of the snowfall. Afterwards, the snowfall weakened and moved to the leeward slope of the Tianshan Mountains at 2000 UTC. At this time, the descending and ascending motions over the peak, the leeward slope and its downstream area enhanced, with the wave extending upwardly to the stratosphere. The gravity waves were featured by the alternate distribution of the ascending and descending motions during the snowfall. The vertical distributions of the horizontal divergence and vertical vorticity (figure omitted) show that the positive and negative-value areas of the vorticity fields distributed alternately in the initial stage of the snowfall at 1330 UTC. The divergence fields presented an upward-tilting development with significant fluctuations. With the eastward movement and the development of the rainfall,

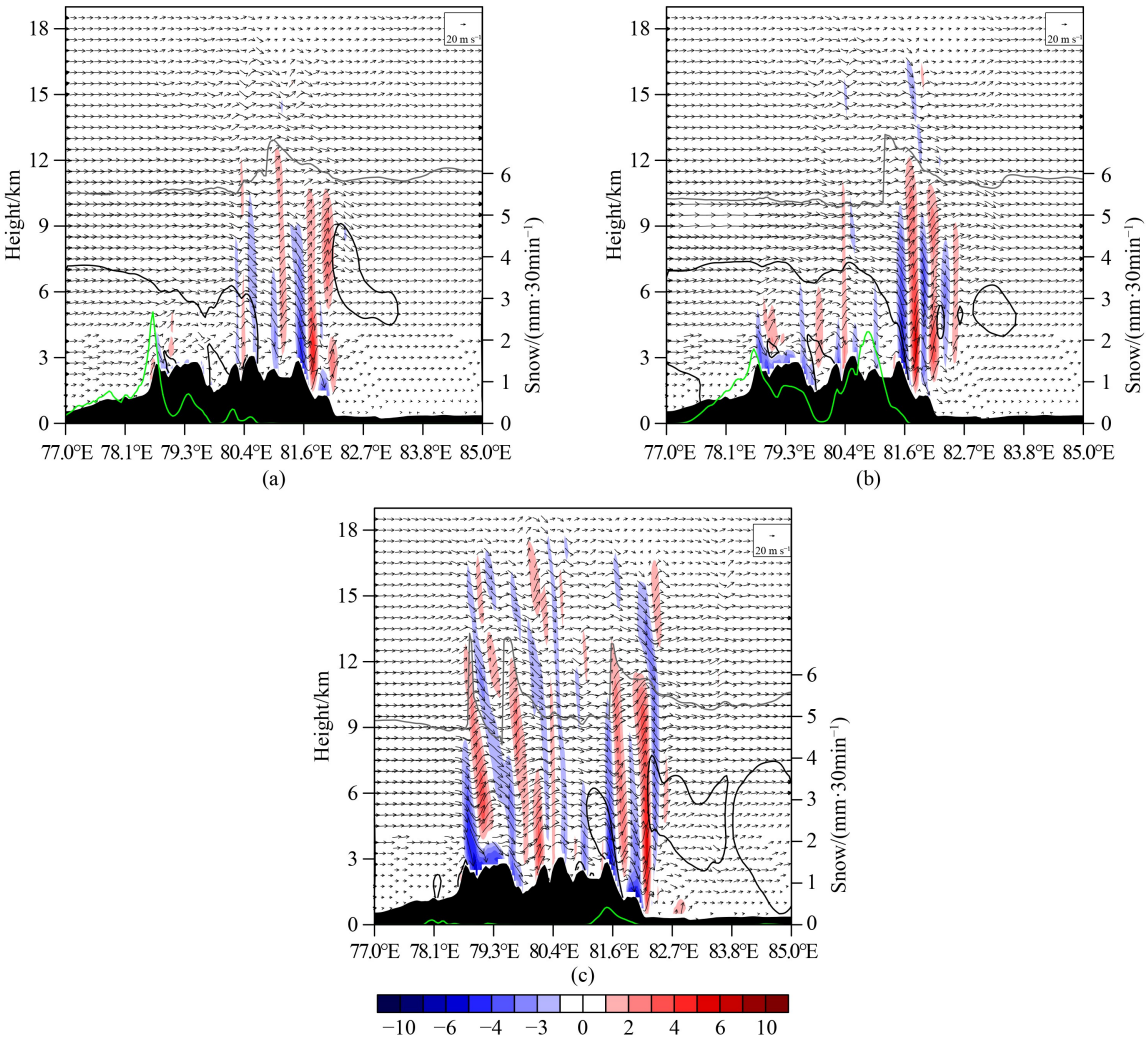

Fig. 2 Cross-sections of the vertical velocity field (shading, units: m·s^{-1}), wind vector (vectors, units: m·s^{-1}), tropopause height (gray solid line, units: km), hydrometeor (contours, units: 10^{-4} kg·kg^{-1}) and 30-min precipitation (green solid line, units: mm) along 44.5°N at (a) 1330 UTC, (b) 1600 UTC and (c) 2000 UTC on November 30, 2018.

the vorticity and divergence fields enhanced with more significant fluctuations at 1600 UTC. Subsequently, the wave propagated upwardly to the stratosphere above and extended westward at 2000 UTC. The anomalous-value area of the vorticity was mainly concentrated over the Tianshan Mountains. According to the horizontal divergence equation in local rectangular coordinates, $\frac{\mathrm{d}D}{\mathrm{d}t} \propto f\varsigma$, the negative vorticity was conducive to the enhancement of the convergence. The anomalous-value areas of the divergence and vorticity extended upwardly, and there was a certain phase difference in their spatial distributions, exhibiting the characteristics of gravity waves.

The complex generation mechanisms for the gravity waves in the atmosphere include orographic uplift, strong convection, vertical shear instability, Wave-CISK mechanism and geostrophic adjustment related to unbalanced flows (Mastrantonio et al., 1976; Lindzen and Tung, 1976; Clark et al., 1986; Koch and Dorian, 1988; Kaplan and Karyampudi, 1992; Bosart et al., 1998; Zhang, 2004). Rossby (1938), Cahn (1945) and Blumen (1972) pointed out that the unbalanced state between the atmospheric mass and momentum fields causes the geostrophic adjustment, which can excite the inertia-gravity waves and radiate away the unbalanced energy. By summarizing the analysis methods for gravity waves, Zhang et al. (2000) pointed out that the Lagrangian Rossby number *Ro* and the residual analysis method of ΔNBE are powerful tools for diagnosing and analyzing the observed atmospheric gravity waves. *Ro* is defined as the ratio of inertial force to Coriolis force, i.e., the relative magnitude of parcel acceleration to Coriolis acceleration (Koch and Dorian, 1988). The equation is as follows:

$$Ro = \frac{|\mathrm{d}\mathbf{V}/\mathrm{d}t|}{f|\mathbf{V}|} = \frac{|f\mathbf{V}_{ag}\times\mathbf{k}|}{f|\mathbf{V}|} \approx \frac{|\mathbf{V}_{ag}^{\perp}|}{|\mathbf{V}|}, \quad (1)$$

where $\mathbf{V}_{ag}^{\perp}$ is the ageostrophic wind, and $\mathbf{V}$ is the total wind speed. The smaller the *Ro* is, the closer the atmosphere is to the quasi-geostrophic balance. The larger the *Ro* is, the stronger the atmospheric ageostrophic motion is. Kaplan et al. (1997) took the *Ro* above 0.7 as the diagnostic criterion for unbalanced state of the atmosphere, where the Coriolis force is equal to the inertial force as proposed by Sun et al. (2012). At that time, the wind direction will be perpendicular to the basic flow, and the wind will obviously deflect, generating significant geostrophic deviation as well as strong convergence and divergence of the airflow. The atmosphere is in an unbalanced state, thus exciting the gravity waves to radiate away the unbalanced energy. Therefore, as an index to judge the ageostrophic state of the atmosphere, the *Ro* can be used to diagnose and analyze the environmental conditions for generating the gravity waves. Figure 3 shows that the *Ro* values in the lower troposphere, the tropopause and the lower stratosphere over the windward slope, the peak and the leeward slope were greater than 0.7 at 1330 UTC, indicating that there were significant ageostrophic motions in the atmosphere. In addition, the high-value areas of *Ro* were mainly located over the leeward slope and its downstream area. During the enhancing stage of the snowfall, the *Ro* gradually increased till 1600 UTC, with its high-value area extending upwardly and the ageostrophic motion becoming stronger, which were conducive to the generation and propagation of gravity waves. During the weakening stage of the snowfall, the *Ro* in the troposphere and lower stratosphere further increased at 2000 UTC. Specially, the high-value areas of *Ro* extended westward in the lower stratosphere, providing a strong ageostrophic condition for the gravity waves propagating eastward or westward.

As revealed by Blumen (1972), when the geostrophic equilibrium state of the atmosphere is destroyed, the convergence and divergence caused by the ageostrophic

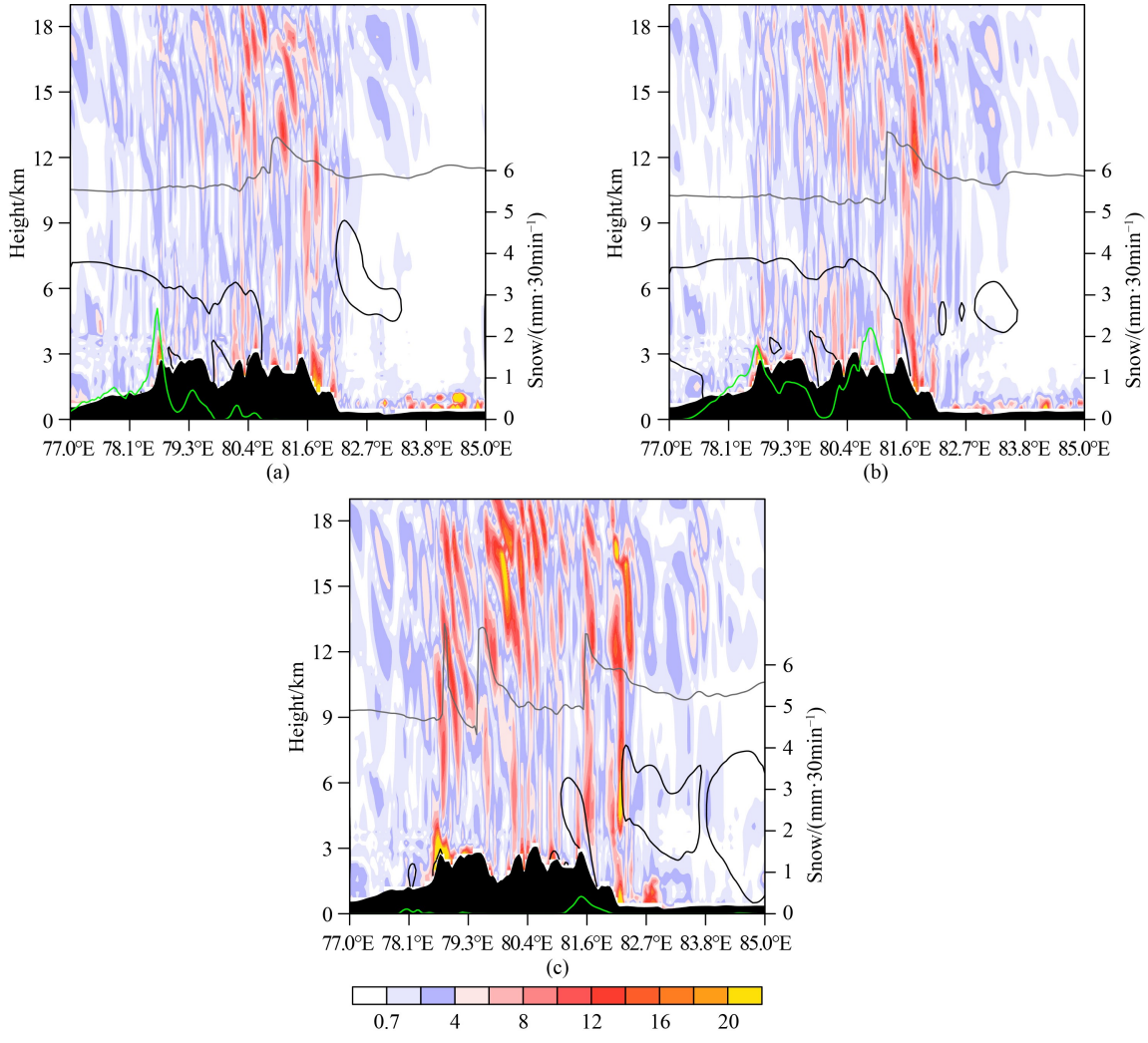

Fig. 3 Cross-sections of *Ro* (shading), tropopause height (gray solid line, units: km), hydrometeor (black solid lines, units: 10^{-4} kg·kg^{-1}) and 30-min precipitation (green solid line, units: mm) along 44.5°N at (a) 1330 UTC, (b) 1600 UTC and (c) 2000 UTC on November 30, 2018.

motion will excite the inertia-gravity waves that redistribute the mass and momentum to establish a new geostrophic equilibrium state. The non-equilibrium state of the atmosphere, i.e., strong convergence and divergence, can be described by the nonlinear balance equation. This equation can be used to analyze whether the unbalanced environmental conditions are favorable for the generation of the gravity waves, which is as follows:

$$\Delta NBE = 2J(u,v) + f\zeta - \beta u - \alpha\nabla^2 p, \quad (2)$$

where $\beta = \partial f/\partial y$, J is the Jacobian operator; P is the air pressure and ξ is the relative vorticity. ΔNBE is the residual of the nonlinear balance equation, which indicates the degree of imbalance for the atmosphere (Zhang, 2004). When the magnitude of ΔNBE is smaller than those of the J, vorticity and Laplacian term on the right side of the equation, the atmosphere is in a quasi-equilibrium state. When the magnitude of ΔNBE is equal to the first three terms on the right side of the equation, the atmosphere is in a non-equilibrium state, and thus the mesoscale inertia-gravity waves with large amplitude may be generated. There were high-value areas of the residual term in the equation in the lower troposphere and tropopause over the peak and the leeward slope of the Tianshan Mountains at 1330 UTC (figure omitted), indicating strong convergence and divergence of the airflow that is conductive to the generation of the inertia-gravity waves. At 1600 UTC, the high-value areas of ΔNBE in the whole troposphere and the low stratosphere intensified, showing an alternate distribution of positive- and negative-value areas, indicating strong convergence and divergence of the atmosphere, which could provide favorable unbalanced conditions for the maintenance and propagation of the gravity waves (Fig. 4(a)). At 2000 UTC, the high-value areas of ΔNBE in the whole

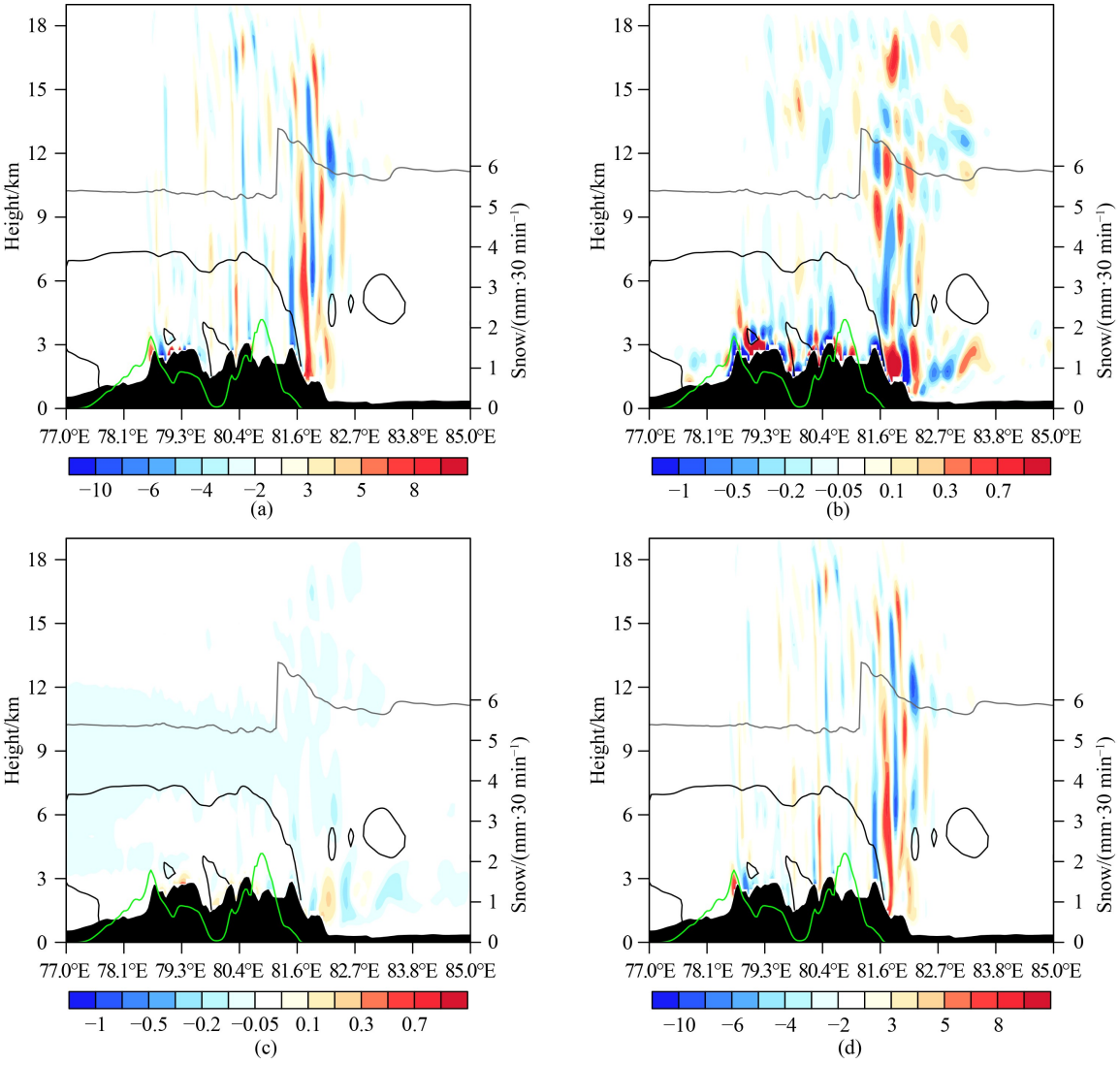

Fig. 4 Cross-sections of (a) ΔNBE, (b) $2J(u,v)$, (c) $f\zeta - \beta u$, (d) $\alpha\nabla^2 P$ (shading, units: 10^{-6} s^{-2}), tropopause height (gray solid line, units: km), hydrometeor (black solid lines, units: 10^{-4} kg·kg^{-1}) and 30-min precipitation (green solid line, units: mm) along 44.5°N at 1600 UTC on November 30, 2018.

troposphere and the low stratosphere over the peak and the leeward slope further strengthened, extending westwardly and upwardly in horizontal and vertical directions, respectively. The strong convergence and divergence of the airflow in a wide range were conducive to the eastward and westward propagation of the gravity waves (figure omitted).

Figure 4 presents the distributions of the terms in the nonlinear balance equation, in which the magnitude of the Laplacian term $-\nabla^2 p$ is the largest, and its distribution is similar to that of the high-value area of ΔNBE, indicating that the high-value areas of the residual term over the peak and the leeward slope is dominated by the Laplacian term $-\nabla^2 p$. The complex topography causes perturbations in the atmospheric pressure and potential temperature fields above, leading to the anomalies in the Laplacian term of the atmospheric pressure. Therefore, the topography is the main factor contributing to the atmospheric unbalanced motion as well as the generation and propagation of gravity waves. Additionally, there is also a high-value area of the Jacobian term in the lower layers over the leeward slope, which demonstrates that the horizontal shear of the wind field also contributes to the unbalanced motion.

The comparison between Fig. 3 and Fig. 4 shows that the high-value areas of both Ro and ΔNBE first appear in the lower layers over the leeward slope, indicating that the generation of the gravity waves is closely related to the topography. In the whole troposphere and lower stratosphere over the peak and the leeward slope, the high-value areas of Ro and ΔNBE are basically consistent, indicating the strong ageostrophy and the imbalance between the convergence and divergence, which creates favorable conditions for the generation and propagation of the gravity waves.

In conclusion, the topographic uplift is strong in this snowfall, and the airflow in the lower layer is forced to rise up due to the topography-induced blocking. When it ascends to the peak and the leeward slope, the fluctuation is generated under the stable stratification, thus forming the inertia-gravity waves. The ageostrophic motion and the unbalanced motion of convergence and divergence in the whole troposphere and the lower stratosphere over the peak and the leeward slope provide favorable conditions for the development of the inertia-gravity waves.

To quantitatively depicting the fluctuating characteristics of the gravity waves, the spectral analysis is first applied to investigate the characteristics for the wavelength and frequency of the gravity waves in the snowfall. For the zonal cross-section along 44.5°N on the northern slope of the Tianshan Mountains, the vertical velocity data of 62 times (interval: 30 min) at the height of 12 km from 0000 UTC on November 30 to 0700 UTC on December 1, 2018 are selected for the FFT. The wave signal at the height of 12 km is very obvious with clear single peak and narrow spectrum. For the high-value area of wave energy density, the wave number ranges from -0.009 km^{-1} to -0.014285 km^{-1} (corresponding to the horizontal wavelength of 70–111 km) and the wave frequency is within 0.0027 min^{-1} and 0.004347 min^{-1} (corresponding to the periods of 230–370 min), indicating typical Meso-β scale waves that propagate eastward and westward. In addition, the eastward-propagating wave energy is stronger, with a phase velocity of about 4–10 m·s^{-1} (Fig. 5). To see if the high-energy wave mentioned above has the feature of polarization, the phase spectrum and coherence spectrum of the vertical vorticity and horizontal divergence are analyzed by the cross spectrum method. According to gravity-wave polarization, the waves can be identified as gravity waves when there is a phase difference of 90° between the vertical vorticity and horizontal divergence. The phase difference between the vertical vorticity and horizontal divergence was about 90° in the wavelength range of 0.009–0.014285 km^{-1} at 2000 UTC on November 30, 2018, which corresponds to high-value coherence spectrum with a characteristic wave number of 0.01425 km^{-1} and a wavelength of about 70.2 km. Therefore, the fluctuations with this wave number are in accord with the polarization feature of the gravity waves, demonstrating that the high-energy fluctuations (the purple arrow in the figure) analyzed above belong to inertia-gravity waves with the wavelength of about 70.2 km, which is also the key scale for gravity waves in this snowfall (Fig. 6).

5 Generation mechanisms for the gravity waves

This section investigates the generation mechanisms for the gravity waves at the key scale (70–111 km) mentioned above. First, the gravity waves with the key scale are separated from the model output, and the non-hydrostatic wave equation are applied in analyzing the sources and sinks of the gravity waves at this scale. In this study, the scale separation is done by the Barnes' filter method,

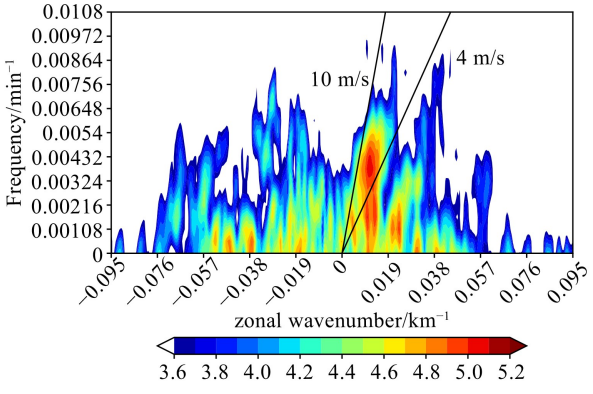

Fig. 5 The power spectral density of the vertical velocity at the height of 12 km along 44.5°N (units: m^2·s^{-2}). The solid lines represent the wave phase velocity of −4 m·s^{-1} and −10 m·s^{-1}.

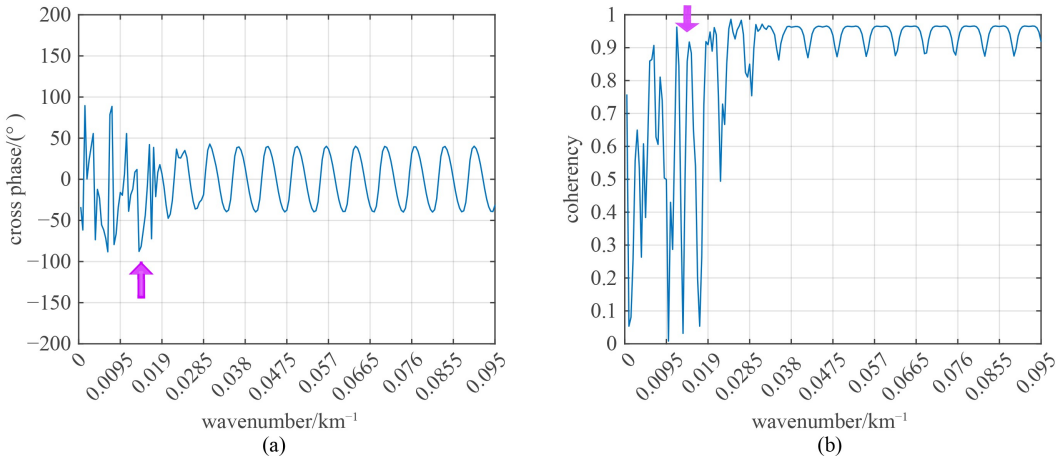

Fig. 6 The (a) phase spectrum and (b) coherence spectrum of the vertical vorticity and the horizontal divergence at the height of 12 km along 44.5°N at 2000 UTC on November 30, 2018.

which is a widely used objective analysis method that can filter out the perturbations at different spatio-temporal scales and retain the background field at a relatively large-scale (Maddox, 1980). Specifically, the formula is as follows:

$$f_0(i,j) = \sum_{n=1}^{N} w_n f_n(x,y) / \sum_{n=1}^{N} w_n, \tag{3}$$

where

$$w_n = \exp(-d_n^2/4c), \tag{4}$$

$$R_0 = \exp(-\pi^2 4c/\lambda^2), \tag{5}$$

$$f(i,j) = f_0(i,j) + \sum_{n=1}^{N} w'_n D_n / \sum_{n=1}^{N} w'_n, \tag{6}$$

$$D_n = f_n(i,j) - f_0(i,j), \tag{7}$$

$$w'_n = \exp(-d_n^2/4gc), \tag{8}$$

$$R = R_0(1 + R_0^{g-1} - R_0^g). \tag{9}$$

The band pass filter and response function are as follows:

$$B(i,j) = r(f_1(i,j) - f_2(i,j)), \tag{10}$$

$$BR = r(R_1 - R_2), \tag{11}$$

where $f_n(x,y)$ is the original meteorological element field; w_n is the weight function; $f_0(i,j)$ is the initial-value filed for filtering; R_0 is the response function; d_n is the distance from $f_n(x,y)$ to the filtering point (i,j); c is the weight coefficient, and N is the number of samples participating the filtering at the point (i,j). $f(i,j)$ is the low-pass filter. The band-pass filter is the difference between the two low-pass filters, that is $B(i,j)$, where r is the reciprocal of the maximum response difference, and BR is the response function of the band-pass filter. The scales of the high-energy gravity waves obtained from the previous analysis are used to determine the filter parameters ($c_1 = 270$, $c_2 = 400$, $g_1 = 0.3$ and $g_2 = 0.4$), and r is set as 3.6. Figure 7 shows the response function of the band-pass filter. The small-scale (below 70 km) and large-scale (above 120 km) fluctuations are filtered out, while the fluctuations with the scale of 70–120 km are retained.

Figure 8 shows the vertical distributions of the vorticity and divergence perturbations after the filtering at the beginning, enhancing and weakening periods of the rainfall. At 1330 UTC, the divergence perturbations presented an upward-tilting development, with the positive- and negative-value areas distributing alternately from the lower to the upper layers. There was a phase difference of about π/2 for the vertical distributions between the vorticity and divergence perturbations, displaying the polarization characteristics of gravity waves. In the development stage of the snowfall, the perturbations on

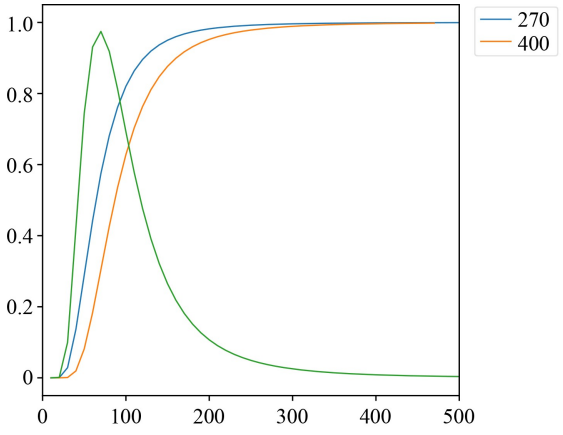

Fig. 7 The band-pass filter response function BR.

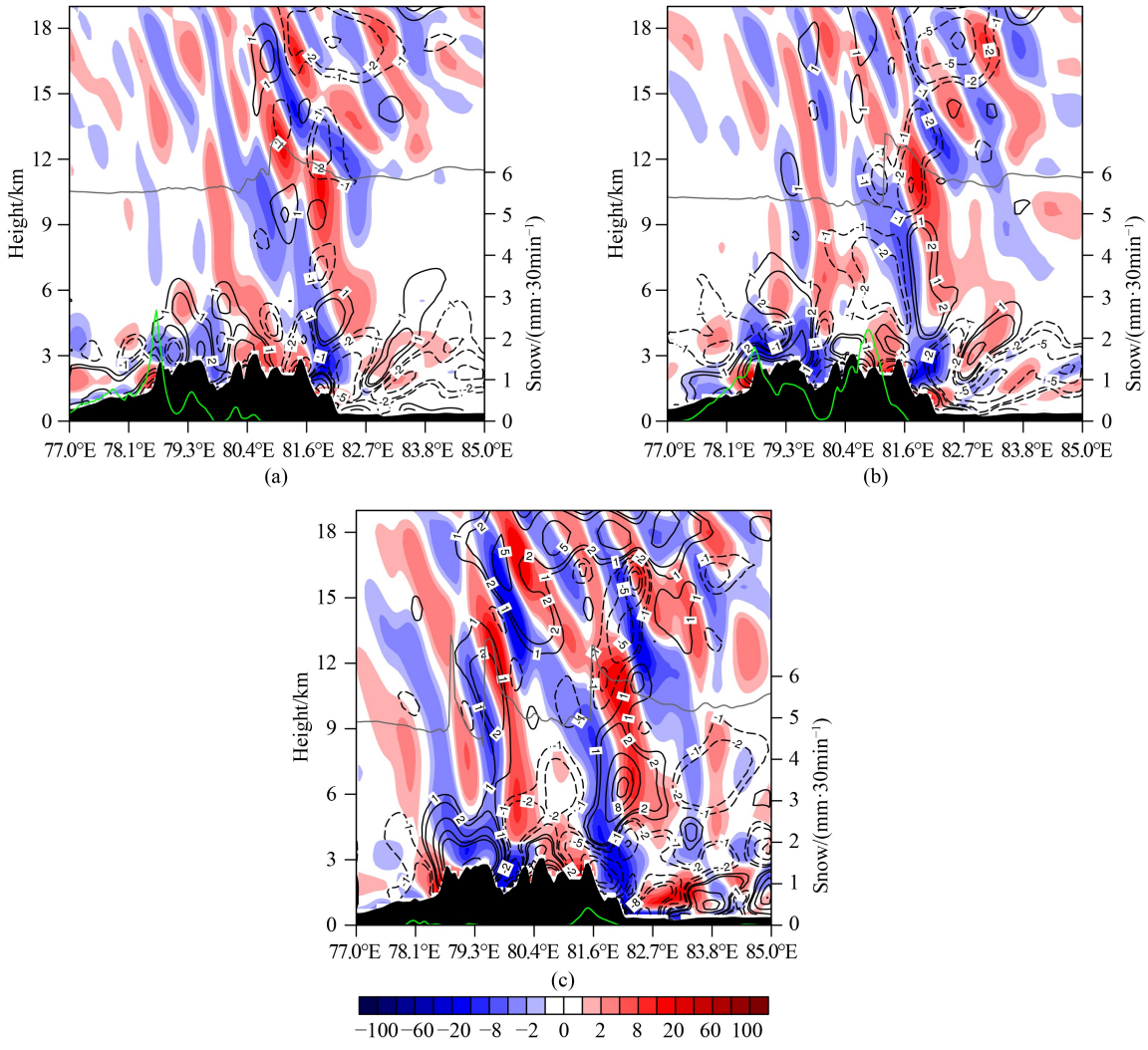

Fig. 8 Cross-sections of the perturbations on the divergence field (shading, units: 10^{-4} s^{-1}) and vorticity field (contours, units: 10^{-4} s^{-1}), the tropopause height (gray solid line, units: km), and 30-min precipitation (green solid line, units: mm) along 44.5°N at (a) 1330 UTC, (b) 1600 UTC and (c) 2000 UTC on November 30, 2018.

vorticity and divergence fields kept enhancing till 1600 UTC, with more obvious fluctuating characteristics. At 2000 UTC, the fluctuation in the lower stratosphere became more significant, and presented a westward extending.

Section 4 shows that there are favorable conditions for the generation and propagation of the gravity waves in the snowfall, and the precipitation over the leeward slope is closely related to the gravity waves. The non-hydrostatic wave equation proposed by Ran and Chen (2016) is adopted here to analyze the forcing terms as well as the sources and sinks for gravity waves. The equation is as follows:

$$-\nabla\frac{\partial^2 w'}{\partial t^2}-N^2\nabla_h^2 w'-f^2\frac{\partial^2 w'}{\partial z^2}=FG0+FG1+FG2+FGS, \tag{12}$$

where

$$FG0=-g\nabla_h^2 FT0+\frac{\partial^2}{\partial z\partial t}FD0+f\frac{\partial}{\partial z}FV0, \tag{13}$$

$$FG1=-g\nabla_h^2 FT1-\nabla_h^2\frac{\partial}{\partial t}FW1+\frac{\partial^2}{\partial z\partial t}FD1+f\frac{\partial}{\partial z}FV1, \tag{14}$$

$$FG2=-g\nabla_h^2 FT2-\nabla_h^2\frac{\partial}{\partial t}FW2+\frac{\partial^2}{\partial z\partial t}FD2+f\frac{\partial}{\partial z}FV2, \tag{15}$$

$$FGS=-g\nabla_h^2 FTS, \tag{16}$$

$$FT0=-\frac{\partial\ln\bar{\theta}}{\partial t}-\bar{v}_h\cdot\nabla\ln\bar{\theta}, \tag{17}$$

$$FT1=-(\frac{\partial\ln\bar{\theta}}{\partial t}+\bar{v}_h\cdot\nabla\ln\bar{\theta})\frac{\theta'}{\bar{\theta}}-v_h'\cdot\nabla\ln\bar{\theta}-\bar{v}_h\cdot\nabla\frac{\theta'}{\bar{\theta}}, \tag{18}$$

$$FT2 = -\frac{\theta'}{\bar{\theta}} v' \cdot \nabla(\ln\bar{\theta}) - v' \cdot \nabla\frac{\theta'}{\bar{\theta}}, \tag{19}$$

$$FTS = \frac{Q}{\theta}, \tag{20}$$

$$FW1 = -\bar{v}_h \cdot \nabla w' - \frac{p'}{\bar{\rho}^2}\frac{\partial\bar{\rho}}{\partial z}, \tag{21}$$

$$FW2 = -v' \cdot \nabla w', \tag{22}$$

$$FD0 = \bar{\varsigma} f + 2\left(\frac{\partial\bar{u}}{\partial x}\frac{\partial\bar{v}}{\partial y} - \frac{\partial\bar{v}}{\partial x}\frac{\partial\bar{u}}{\partial y}\right), \tag{23}$$

$$\begin{aligned} FD1 =& \bar{v}_h \cdot \nabla\left(\frac{\partial w'}{\partial z}\right) + 2\left(\frac{\partial\bar{u}}{\partial x}\frac{\partial v'}{\partial y} - \frac{\partial v'}{\partial x}\frac{\partial\bar{u}}{\partial y} + \frac{\partial u'}{\partial x}\frac{\partial\bar{v}}{\partial y} - \frac{\partial\bar{v}}{\partial x}\frac{\partial u'}{\partial y}\right) \\ & - \left(\frac{\partial w'}{\partial x}\frac{\partial\bar{u}}{\partial z} + \frac{\partial w'}{\partial y}\frac{\partial\bar{v}}{\partial z}\right), \end{aligned} \tag{24}$$

$$\begin{aligned} FD2 =& v' \cdot \nabla\left(\frac{\partial w'}{\partial z}\right) + 2\left(\frac{\partial u'}{\partial x}\frac{\partial v'}{\partial y} - \frac{\partial v'}{\partial x}\frac{\partial u'}{\partial y}\right) \\ & - \left(\frac{\partial w'}{\partial x}\frac{\partial u'}{\partial z} + \frac{\partial w'}{\partial y}\frac{\partial v'}{\partial z}\right) - \left(\frac{\partial w'}{\partial z}\right)^2, \end{aligned} \tag{25}$$

$$FV0 = -\frac{\partial\bar{\varsigma}}{\partial t} - \bar{v}_h \cdot \nabla\bar{\varsigma}, \tag{26}$$

$$FV1 = -\bar{v}_h \cdot \nabla\varsigma' - v' \cdot \nabla\bar{\varsigma} + \bar{\varsigma}\left(\frac{\partial w'}{\partial z}\right) - \frac{\partial w'}{\partial x}\frac{\partial\bar{v}}{\partial z} + \frac{\partial w'}{\partial x}\frac{\partial\bar{u}}{\partial z}, \tag{27}$$

$$FV2 = -v' \cdot \nabla\varsigma' + \varsigma'\frac{\partial w'}{\partial z} - \frac{\partial w'}{\partial x}\frac{\partial v'}{\partial z} + \frac{\partial w'}{\partial x}\frac{\partial u'}{\partial z}. \tag{28}$$

Table 2 shows the physical meanings of the terms and components in the non-hydrostatic wave equation. The left- hand side of Eq. (12) shows the operator of the gravity waves, and the right end shows the forcing terms, including the basic state term, first-order linear term, second-order nonlinear term and thermodynamic term. If the forcing term on the right- hand side is zero, the left operator can be transformed to the dispersion relation of gravity waves, which represents stable gravity waves. If the forcing term on the right- hand side is not zero, this equation describes the unstable gravity waves, and the wave amplitude is evolving.

Figure 9 shows that in the enhancing stage of the rainfall, the four forcing terms of the gravity waves fluctuated with an alternate distribution of positive and negative centers from the lower to the upper layers. Among the four forcing terms, the second-order nonlinear term is the most important, followed by the thermodynamic term. The first-order linear term is slightly smaller, and the basic state term is one order of magnitude smaller than those of other three terms, which thus can be basically ignored. The high-value area of the second-order nonlinear term is mainly located near the surface of the peak, while it is located in the whole troposphere and the lower stratosphere over the leeward slope, with a more significant forcing effect in the lower layer. The high-value area of thermal forcing term is mainly located over the windward slope, the peak, the leeward slope, and the middle and lower troposphere downstream, corresponding to the cloud that is mainly caused by the release of the condensation latent heat. The high-value area of the first-order linear term is mainly concentrated in the lower troposphere, tropopause and lower stratosphere over the peak and the leeward slope, which is mainly related to the coupling of large-scale and mesoscale gravity waves.

Table 2 Physical meanings for the terms in Eqs. (13)–(28)

Terms and components of the non-hydrostatic wave equation	Physical meanings
$FG0$	Basic state term
$FG1$	First-order linear forcing term
$FG2$	Second-order nonlinear forcing term
FGS	Thermodynamic term
$FT0$	Forcing term for the basic state of potential temperature
$FT1$	Linear forcing term for potential temperature
$FT2$	Quadratic forcing term for potential temperature
FTS	Adiabatic forcing term
$FW1$	Linear forcing term for vertical velocity
$FW2$	Quadratic forcing term for vertical velocity
$FD0$	Forcing term for the basic state of the divergence
$FD1$	Linear forcing term for divergence
$FD2$	Quadratic forcing term for divergence
$FV0$	Forcing term for the basic state of the vertical vorticity
$FV1$	Linear forcing term for vertical vorticity
$FV2$	Quadratic forcing term for vertical vorticity

The further analysis of the second-order nonlinear term $FG2$ (Fig. 10) shows that its magnitude is mainly determined by the nonlinear thermal forcing term $-g\nabla_h^2 FT2$, whose high-value areas are located in the whole troposphere and the lower stratosphere over the leeward slope, followed by the nonlinear dynamic divergence term $\frac{\partial^2}{\partial z\partial t}FD2$. This term mainly contributes to the term of $FG2$ in the lower troposphere over the peak and the leeward slope (figure omitted), while the other terms contribute slightly. The magnitude of $FT2$ mainly depends on the disturbance advection transport of the potential temperature perturbations, i.e., $-v' \cdot \nabla\frac{\theta'}{\bar{\theta}}$

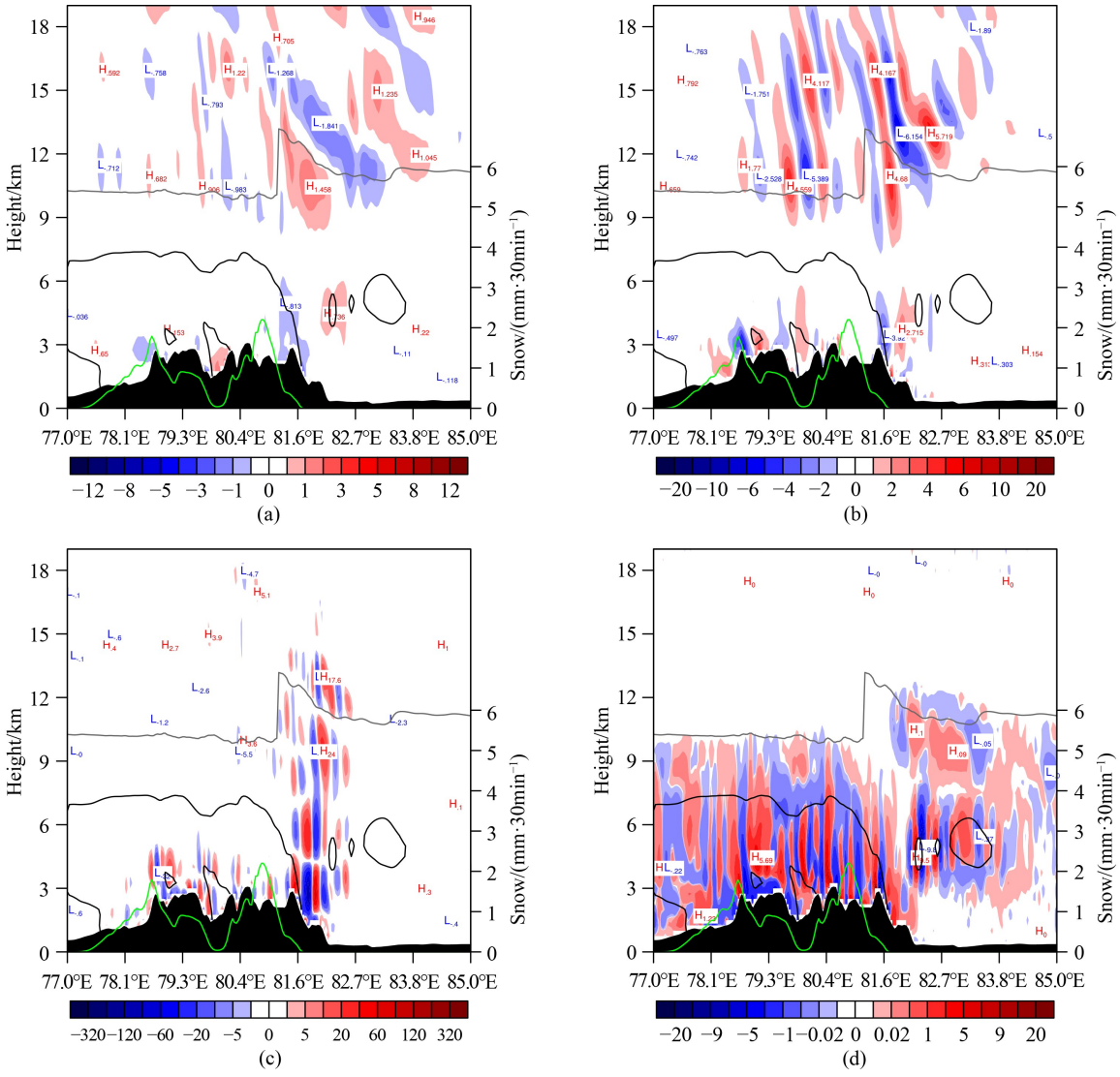

Fig. 9 Cross-sections of the (a) basic state term (shading, units: 10^{-13} m^{-1}·s^{-3}), (b) first-order linear term (units: 10^{-12} m^{-1}·s^{-3}), (c) second-order nonlinear term (units: 10^{-12} m^{-1}·s^{-3}), (d) thermodynamic term (units: 10^{-12} m^{-1}·s^{-3}), tropopause height (gray solid line, units: km), hydrometeor (contours, units: 10^{-4} kg·kg^{-1}) and precipitation (green solid line, units: mm) along 44.5°N at 1600 UTC on November 30, 2018.

(Fig. 10(b)). This term can be decomposed into $-u_e\frac{\partial\frac{\theta'}{\bar{\theta}}}{\partial x}-v_e\frac{\partial\frac{\theta'}{\bar{\theta}}}{\partial y}-w_e\frac{\partial\frac{\theta'}{\bar{\theta}}}{\partial y}$, where the vertical transport of the potential temperature perturbations, $-w_e\frac{\partial\frac{\theta'}{\bar{\theta}}}{\partial z}$, has anomalous high values in the whole troposphere and the lower stratosphere over the leeward slope, and it is similar to the second-order nonlinear term in the vertical structure, indicating that the vertical transport of the thermal perturbations is the main reason for the anomalies of the second-order nonlinear term. The thermal perturbation $\frac{\theta'}{\bar{\theta}}$ essentially represents the buoyancy $\left(\frac{\theta'}{\bar{\theta}}g\right)$, and it is rather strong in the lower troposphere and lower stratosphere over the mountainous area, as shown in Fig. 11. Over the leeward slope, the potential temperature perturbations present an alternate distribution of positive and negative centers from the lower troposphere to the lower stratosphere. At the same time, the vertical velocity perturbations w_e over the leeward slope are so strong that there is a strong vertical advection of the potential temperature perturbations in the whole troposphere and stratosphere on the leeward slope. Over the mountainous area, especially over the leeward slope, the potential temperature fluctuates greatly, which is mainly due to the topographic relief. Meanwhile, the release of the condensation latent heat of the snowfall area in the middle and lower troposphere also leads to the potential temperature fluctuations. Thus, the topographic forcing and the condensation latent heating together cause the potential temperature perturbations. The transportation of

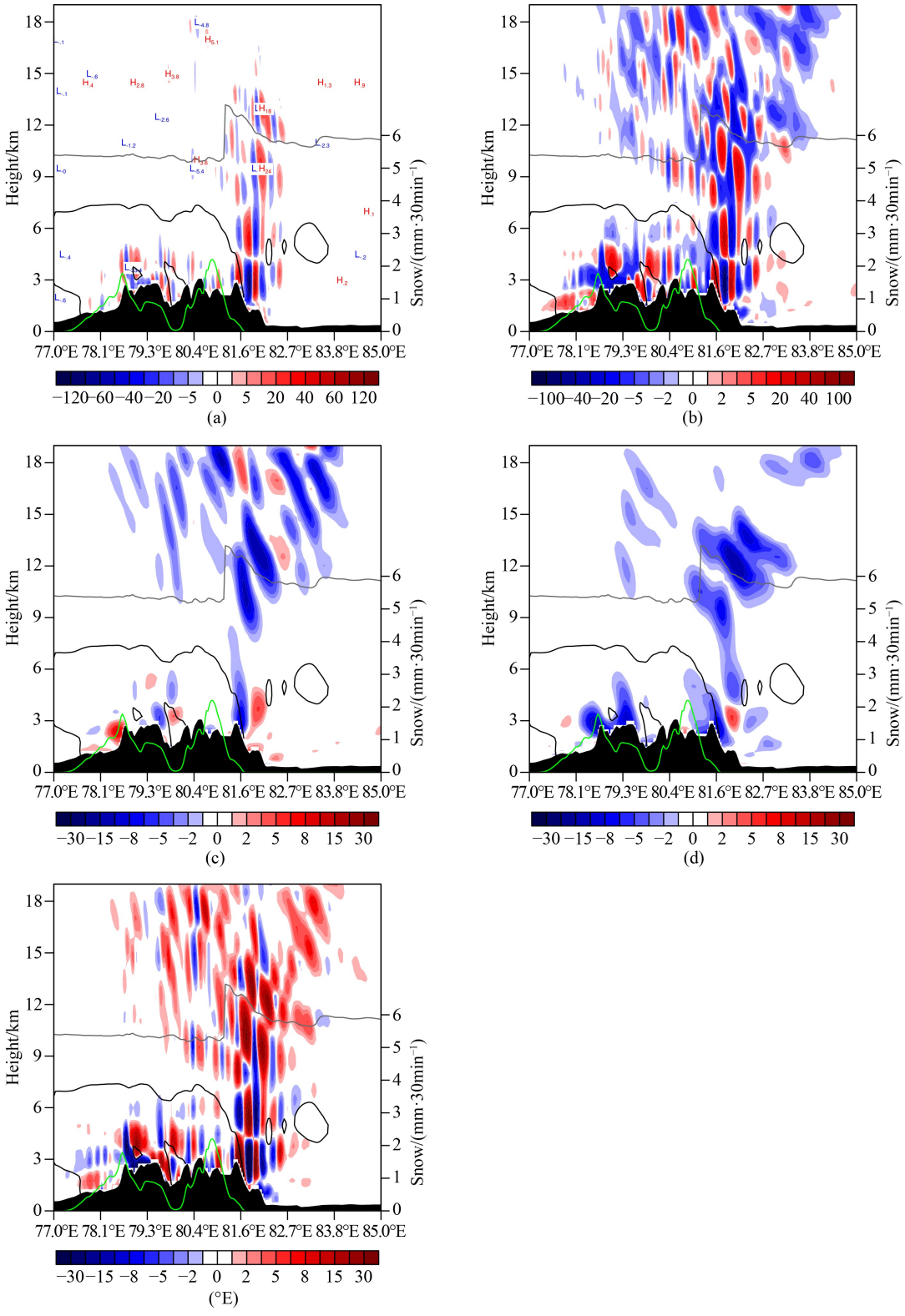

Fig. 10 Cross-sections of the (a) $-g\nabla_h^2 FT2$ (shading, units: 10^{-12} m^{-1}·s^{-3}), (b) $-v'\cdot\nabla\frac{\theta'}{\bar{\theta}}$ (shading, units: 10^{-5} s^{-1}), (c) $-u_e\frac{\partial\frac{\theta'}{\bar{\theta}}}{\partial x}$ (shading, units: 10^{-6} s^{-1}), (d) $-v_e\frac{\partial\frac{\theta'}{\bar{\theta}}}{\partial y}$ (shading, units: 10^{-6} s^{-1}), (e) $-w_e\frac{\partial\frac{\theta'}{\bar{\theta}}}{\partial y}$ (shading, units: 10^{-6} s^{-1}), tropopause height (gray solid line, units: km), hydrometeor (contours, units: 10^{-4} kg·kg^{-1}), and precipitation (green solid line, units: mm) along 44.5°N at 1600 UTC on November 30, 2018.

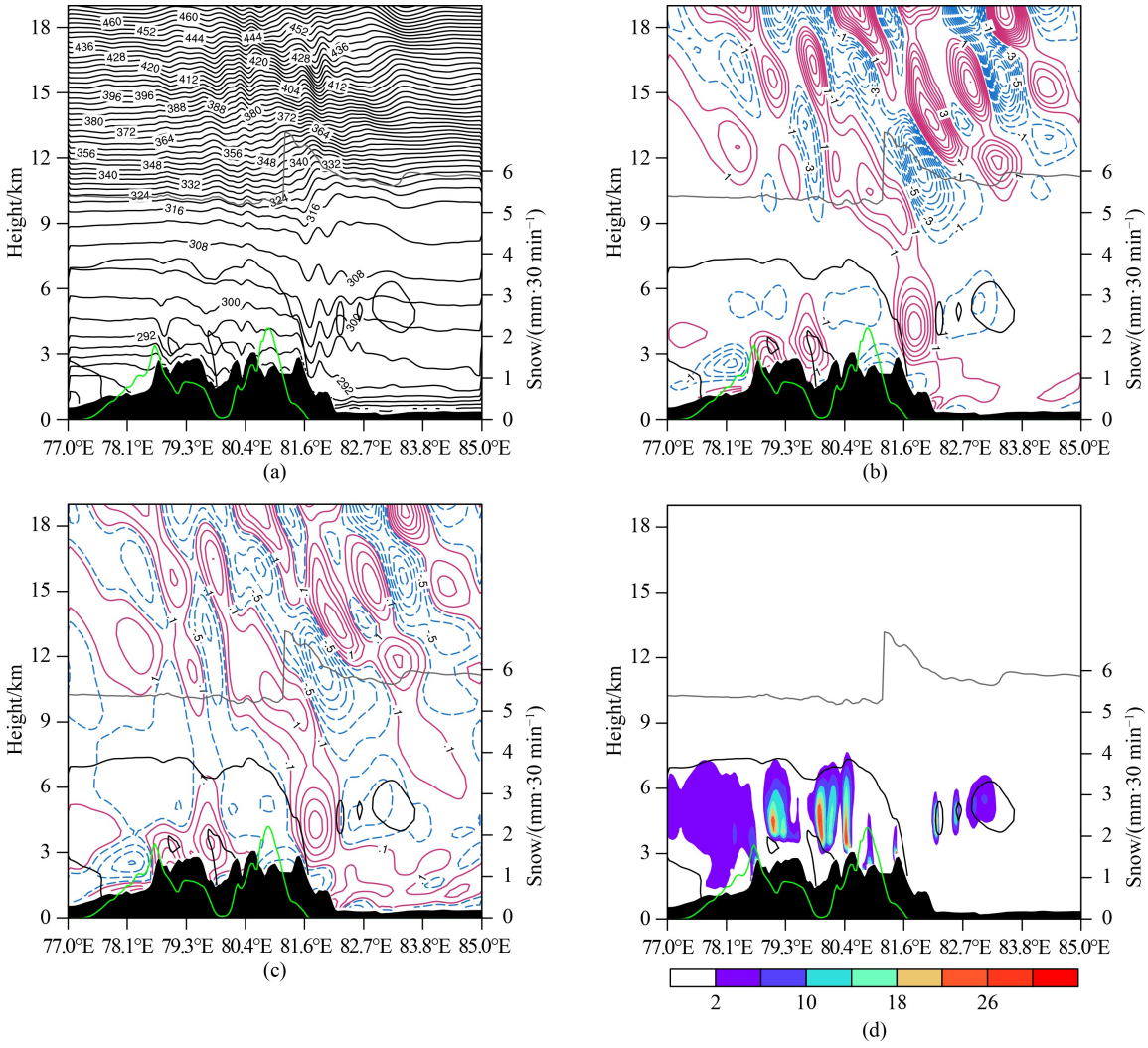

Fig. 11 Cross-sections of the (a) potential temperature θ (contours, units: K), (b) potential temperature perturbation θ' (contours, units: K), (c) $\frac{\theta'}{\theta}$ (contours), (d) latent heat during the microphysical processes (shading, units: 10^{-4} K s^{-1}), tropopause height (gray solid line, units: km), hydrometeor (contours, units: 10^{-4} kg·kg^{-1}) and precipitation (green solid line, units: mm) along 44.5°N at 1600 UTC on November 30, 2018.

the vertical advection of perturbations leads to the nonlinear thermal forcing, causing the generation of gravity waves in the snowfall. Besides, the most significant gravity waves appear over the leeward slope due to the strongest potential temperature perturbations and the largest buoyancy there.

6 Conclusions

In this study, the simulations of the snowstorm over the Ili Valley and the northern slope of the Tianshan Mountains on November 30, 2018 by the WRF model are used to analyze the mesoscale gravity waves and corresponding relationship with the precipitation during the snowfall. The vertical motion is strong when the airflow passes over the mountain, especially, the ascending and descending motions over the leeward slope are rather intense. With the weakening and eastward movement of the snowfall, the vertical motion over the mountain gradually strengthens. When the snowfall gradually weakens and moves eastward to the leeward slope, the ascending and descending motions over the leeward slope and its rear side gradually enhance with time. It is an important feature of the gravity waves that the ascending and descending motions distribute alternately during the snowfall. The positive- and negative-value areas on vorticity and divergence fields are densely and alternatively distributed. During the development of the snowfall, the divergence demonstrates an upward-tilting development, presenting an alternate distribution of positive- and negative-value areas from the lower layers to the upper layers with significant fluctuations. The anomalous-value areas of the vorticity are mainly concentrated over the Tianshan Mountains. According to the horizontal divergence equation in local

rectangular coordinates, i.e., $\frac{\mathrm{d}D}{\mathrm{d}t} \propto f\varsigma$, the negative vorticity is conducive to the enhancement of the convergence. The upward-tilting vorticity exhibits the characteristics of the gravity waves.

In general, the unbalanced state between the atmospheric mass and momentum fields would cause the generation of the gravity waves. The *Ro* and nonlinear balance equation are usually used to diagnose the non-equilibrium of the atmosphere. The results show that the extreme *Ro* values are mainly located over the leeward slope and its rear side, which is conducive to exciting the gravity waves. With the development of the snowfall, the *Ro* increases gradually. The high-value area of ΔNBE gradually strengthens with the development of the precipitation, showing an alternate distribution of positive and negative centers and extending upwardly, which is conducive to the maintenance and upward propagation of the gravity waves. The high-value areas of ΔNBE and *Ro* are basically consistent, representing the features of strong ageostrophy and non-equilibrium between the convergence and the divergence, which is closely related to the generation and propagation of the gravity waves. In addition, both *Ro* and ΔNBE first develop in the lower layers over the leeward slope, which indicates that the generation of the gravity waves is closely related to the topography. During this snowfall, the air parcel in the lower layer is forced to rise up due to the strong effect from topographic uplift. When the airflow ascends to the peak and the leeward slope, the fluctuations are generated under the stable stratification, and thus the inertia-gravity waves are formed. The ageostrophic motion and the unbalanced motion between convergence and divergence in the whole troposphere and the lower stratosphere over the peak and the leeward slope provide favorable conditions for the development of the inertia-gravity waves.

The quantitative analysis by the FFT method shows that the wave signal is the most obvious at the height of 12 km. For high-value areas of wave energy density, the wave number is between $-0.009\ \mathrm{km}^{-1}$ and $-0.014285\ \mathrm{km}^{-1}$ (corresponding to the horizontal wavelength of 70–111 km) and the wave frequency is between $0.0027\ \mathrm{min}^{-1}$ and $0.004347\ \mathrm{min}^{-1}$ (corresponding to the period of 230–370 min), indicating typical meso-β scale gravity waves. The gravity waves propagate both eastward and westward, with the eastward-propagating phase velocity being about $4–10\ \mathrm{m\cdot s}^{-1}$. In addition, the cross spectrum analysis shows that the wavelength of about 70 km for gravity waves is the key scale for fluctuations in this snowfall. In terms of the horizontal scale of gravity waves obtained by the FFT, the Barnes' band-pass filter is utilized to separate the mesoscale fluctuation and the synoptic-scale basic flow. Results show that there is a phase difference of about $\pi/2$ between the vertical distributions of the vorticity and divergence perturbations, presenting the polarization state of gravity waves. The analysis on the forcing terms of the gravity waves by the non-hydrostatic wave equation shows that the main forcing terms of the orographic gravity waves are $FT2$ and $F\mathrm{T}2$, where the largest contribution comes from $F\mathrm{T}2$, with its magnitude mainly depending on $-g\nabla_h^2 FT2$. The term $-g\nabla_h^2 FT2$ is mainly related to the vertical transport of the potential temperature perturbations. During the snowfall, the potential temperature perturbations are mainly caused by the topographic relief and the latent heat release. Thus, the topographic forcing and condensation latent heating together cause the gravity waves in the snowfall. The strongest potential temperature perturbations and the largest buoyancy over the leeward slope result in the most significant gravity waves there.

Acknowledgments This work was supported by the National Key Research and Development Project (No. 2018YFC1507104), Strategic Priority Research Program of the Chinese Academy of Sciences (No. XDA17010105), The Key Scientific and Technology Research and Development Program of Jilin Province (No. 20180201035SF), and National Natural Science Foundation of China (Grant No. 41775140). We thank Nanjing Hurricane Translation for reviewing the English language quality of this paper.

References

Berckmans J, Woollings T, Demory M E, Vidale P L, Roberts M (2013). Atmospheric blocking in a high resolution climate model: influences of mean state, orography and eddy forcing. Atmos Sci Lett, 14(1): 34–40

Blumen W (1972). Geostrophic adjustment. Rev Geophys, 10(2): 485–528

Bosart L F, Bracken W E, Seimon A (1998). A study of cyclone mesoscale structure with emphasis on a large-amplitude inertia-gravity wave. Mon Weather Rev, 126(6): 1497–1527

Bruintjes R T, Clark T L, Hall W D (1994). Interactions between topographic airflow and cloud/precipitation development during the passage of a winter storm in Arizona. J Atmos Sci, 51(1): 48–67

Cahn A (1945). An investigation of the free oscillations of a simple current system. J Atmos Sci, 2(2): 113–119

Clark T L, Hauf T H, Kuettner J P (1986). Convectively forced internal gravity waves: results from two-dimensional numerical experiments. Q J R Meteorol Soc, 112(474): 899–925

Eliassen A, Palm E (1960). On the transfer of energy in stationary mountain waves. Geofys Publ, 22(3): 1–23

Ford R (1994). Gravity wave radiation from vortex trains in rotating shallow water. J Fluid Mech, 281(25): 81–118

Fritts D C, Alexander M J (2003). Gravity wave dynamics and effects in the middle atmosphere. Rev Geophys, 41(1): 1003

Garvert M F, Smull B, Mass C (2007). Multiscale mountain waves influencing a major orographic precipitation event. J Atmos Sci, 64(3): 711–737

Guan X F, Sun W G, Li M J, Xie C Y, Zhang X Q (2016). Climate change in north Xinjiang and its response to Arctic Oscillation during the period of 1965–2012. Arid Zone Res, 33(04): 681–689 (in Chinese)

Guo X, Guo X L, Fu D H, Niu S J (2013). Relationship between bell-shaped terrain dynamic forcing, mountain wave propagation, and

orographic clouds and precipitation. Chin J Atmos Sci, 37(4): 786−800 (in Chinese)

Holton J R, Haynes P H, McIntyre M E, Douglass A R, Rood R B, Pfister L (1995). Stratosphere–troposphere exchange. Rev Geophys, 33(4): 403–439

Houze R A Jr (2012). Orographic effects on precipitating clouds. Rev Geophys, 50(1): RG1001

Howard L N (1961). Note of a paper of John W. Miles. J Fluid Mech, 10(4): 509–512

Kanehama T, Sandu I, Beljaars A, van Niekerk A, Lott F A (2019). Which orographic scales matter most for medium-range forecast skill in the Northern Hemisphere winter? J Adv Model Earth Syst, 11(12): 3893–3910

Kaplan M L, Karyampudi V M (1992). Meso-bata scale numerical simulations of terrain drag-induced along-stream circulations. Part II: concentration of potential vorticity within dryline bulges. Meteorol Atmos Phys, 49(1−4): 157–185

Kaplan M L, Koch S E, Lin Y L, Weglarz R P, Rozumalski R A (1997). Numerical simulations of a gravity wave event over CCOPE. Part I: the role of geostrophic adjustment in mesoscale jetlet formation. Mon Weather Rev, 125(6): 1185–1211

Kim Y J, Eckermann S D, Chun H Y (2003). An overview of the past, present and future of gravity-wave drag parameterization for numerical climate and weather prediction models. Atmos-ocean, 41(1): 65–98

Koch S E, Dorian P B (1988). A mesoscale gravity wave event observed during CCOPE. Part III: wave environment and probable source mechanisms. Mon Weather Rev, 116(12): 2570–2592

Lindzen R S (1974). Wave-CISK in the tropics. J Atmos Sci, 31(1): 156–179

Lindzen R S, Tung K K (1976). Banded convective activity and ducted gravity waves. Mon Weather Rev, 104(12): 1602–1617

Liu L, Ding Z Y, Chang Y, Chen M Q (2012). Application of parameterization of orographic gravity wave drag in WRF model to mechanism analysis of a heavy rain in warm sector over south China. J Meteor Sci, 40(02): 232−240 (in Chinese)

Ma S P, Ran L K, Cao J (2021). Diagnosis and analysis of vertical motion during complex topographical heavy snowfall. Chin J Atmos Sci, 45(5): 1127−1145 (in Chinese)

Maddox R A (1980). An objective technique for separating macroscale and mesoscale features in meteorological data. Mon Weather Rev, 108(8): 1108–1121

Mastrantonio G, Einaudi F, Fua D, Lalas D P (1976). Generation of gravity waves by jet streams in the atmosphere. J Atmos Sci, 33(9): 1730–1738

Medina S, Smull B F, Houze J R R A Jr, Steiner M (2005). Cross-barrier flow during orographic precipitation events: results from MAP and IMPROVE. J Atmos Sci, 62(10): 3580–3598

Miles J W (1961). On the stability of heterogeneous shear flows. J Fluid Mech, 10(4): 496–508

O'sullivan D, Dunkerton T J (1995). Generation of inertia–gravity waves in a simulated life cycle of baroclinic instability. J Atmos Sci, 52(21): 3695–3716

Pandya R E, Durran D R, Weisman M L (2000). The influence of convective thermal forcing on the three-dimensional circulation around squall lines. J Atmos Sci, 57(1): 29–45

Plougonven R, Zhang F Q (2007). On the forcing of inertia–gravity waves by synoptic-scale flows. J Atmos Sci, 64(5): 1737–1742

Ran L K, Chen C S (2016). Diagnosis of the forcing of inertial-gravity waves in a severe convection system. Adv Atmos Sci, 33(11): 1271–1284

Rossby C G (1938). On the mutual adjustment of pressure and velocity distributions in certain simple current systems II. J Mar Res, 1(3): 239–263

Sandu I, van Niekerk A, Shepherd T G, Vosper S B, Zadra A, Bacmeister J, Beljaars A, Brown A R, Dörnbrack A, McFarlane N, Pithan F, Svensson G (2019). Impacts of orography on large-scale atmospheric circulation. Clim Atmosph Sci 2: 10

Shang S S, Lian L Z, Ma T, Zhang K, Han T (2018). Spatiotemporal variation of temperature and precipitation in northwest China in recent 54 years. Arid Zone Res, 35(01): 68–76

Siler N, Roe G, Durran D (2013). On the dynamical causes of variability in the rain-shadow effect: a case study of the Washington Cascades. J Hydrometeorol, 14(1): 122–139

Skamarock W C, Klemp J B, Dudhia J, Gill D O, Liu Z Q, Berner J, Wang W, Powers J G, Duda M G, Huang X Y (2019). A description of the advanced research WRF Version 4. NCAR Tech. Note NCAR/TN-556+STR.

Song I S, Chun H Y, Lane T P (2003). Generation mechanisms of convectively forced internal gravity waves and their propagation to the stratosphere. J Atmos Sci, 60(16): 1960–1980

Sun Y H, Li Z C, Shou S W (2012). A mesoscale analysis of the snowstorm event of 3–5 March 2007 in Liaoning Province. Acta Meteorol Sin, 70(5): 936−948 (in Chinese)

van Niekerk A, Shepherd T G, Vosper S B, Webster S (2016). Sensitivity of resolved and parametrized surface drag to changes in resolution and parametrization. Q J R Meteorol Soc, 142(699): 2300–2313

Vosper S B, van Niekerk A, Elvidge A, Sandu I, Beljaars A (2020). What can we learn about orographic drag parametrisation from high-resolution models? A case study over the Rocky Mountains. Q J R Meteorol Soc, 146(727): 979–995

Wang S G, Zhang F Q (2010). Source of gravity waves within a vortex-dipole jet revealed by a linear model. J Atmos Sci, 67(5): 1438–1455

Wang X, Chu C J, Mou H (2020). Spatial pattern and interannual variation characteristics of snow disaster in Xinjiang. Arid Zone Res, 37(6): 1488−1495 (in Chinese)

Yang R, Liu Y, Ran L K, Zhang Y L (2018). Simulation of a torrential rainstorm in Xinjiang and gravity wave analysis. Chin Phys B, 27(5): 059201

Zhang F Q, Koch S E, Davis C A, Kaplan M (2000). A survey of unbalanced flow diagnostics and their application. Adv Atmos Sci, 17(2): 165–183

Zhang F Q, Davis C A, Kaplan M L, Koch S E (2001). Wavelet analysis and the governing dynamics of a large-amplitude mesoscale gravity-wave event along the east coast of the United States. Q J R Meteorol Soc, 127(577): 2209–2245

Zhang F Q (2004). Generation of mesoscale gravity waves in upper-tropospheric jet-front systems. J Atmos Sci, 61(4): 440–457

Zhang J B, Deng Z F (1987). Introduction to Xinjiang Precipitation. Beijing: Meteorological Press (in Chinese)

Zhu M, Yu Z H, Lu H C (1999). The effect of meso-scale lee wave and its application. Acta Meteorol Sin, 57(6): 705−714 (in Chinese)